Investigation of TiO2 thin film deposited by microwave plasma assisted sputtering and its application in 3D glasses

Hao, Qi; Xiuhua, Fu; Song, Shigeng; Gibson, Desmond; Li, Cheng; Chu, Hin On; Shi, Yongjing

Published in:
COATINGS

Published: 02/08/2018

Document Version
Publisher's PDF, also known as Version of record

coatings

MDPI

Article

Investigation of TiO_2 Thin Film Deposited by Microwave Plasma Assisted Sputtering and Its Application in 3D Glasses

Qi Hao [1], Xiuhua Fu [1,*], Shigeng Song [2,*], Des Gibson [2], Cheng Li [2], Hin On Chu [2] and Yongjing Shi [3]

1 School of OptoElectronic Engineering, Changchun University of Science and Technology, Changchun 130022, China; HaoQi717@outlook.com
2 Institute of Thin Films, Sensors and Imaging, School of Engineering and Computing, University of the West of Scotland, PA1 2BE Paisley, UK; Des.Gibson@uws.ac.uk (D.G.); Cheng.Li@uws.ac.uk (C.L.); Hinon.Chu@uws.ac.uk (H.O.C.)
3 School of Material Science and Engineering, Chongqing University of Science and Technology, Chongqing 401331, China; yjshi@126.com
* Correspondence: fuxiuhua@cust.edu.cn (X.F.); shigeng.song@uws.ac.uk (S.S.); Tel.: +44-141-848-3630 (S.S.)

Received: 2 July 2018; Accepted: 31 July 2018; Published: 2 August 2018

Abstract: TiO_2 deposition using separate regions for sputtering and oxidation is not well investigated. We optimized process parameter for such as oxygen flow and microwave power to produce high quality TiO_2 filters for Stereo/3D imaging applications. This deposition technique was chosen for its unique advantages: high deposition rates while increasing the probability of obtaining stoichiometric oxides, reduces possibility of target poisoning and provides better stability of process. Various characterization methods, such as scanning electron microscopy (SEM), atomic force microscopy (AFM), Raman, X-ray diffraction (XRD), transmission spectroscopy, were used in compliment to simulations for detailed analysis of deposited TiO_2 thin films. Process parameters were optimized to achieve TiO_2 films with low surface scattering and absorption for fabricating multi-passbands interference filter for 3D glasses. From observations and quantitative analysis of surfaces, it was seen that surface roughness increases while oxygen flow or microwave power increases. As the content of anatase phase also increases with higher microwave power and higher oxygen flow, the formation of anatase grains can cause higher surface roughness. Optical analysis of samples validates these trends and provided additional information for absorption trends. Optimized parameters for deposition process are then obtained and the final fabricated 3D glasses filters showed high match to design, within 0.5% range for thickness error.

Keywords: TiO_2; thin films; microwave plasma enhanced sputtering; process optimization; interference optical filter; 3D glasses

1. Introduction

Titanium oxide (TiO_2) thin films have a wide range of applications due to their unique optical, physical, chemical and electronic properties, for example: solar cells [1], photocatalysis [2], gas sensors [3] antireflective coatings [4], self-surface clean [5], antibacterial [6] and so forth.

TiO_2 is a n-type semiconductor with a wide energy band gap and high refractive index with structural forms of amorphous, rutile, anatase and brookite (or mixtures); rutile is the most stable phase among these structures. The electronic and optical properties of TiO_2 film has be widely investigated experimentally [7] and theoretically [8]. As reported, Rutile has a direct forbidden gap (3.03 eV), which is almost degenerate with an indirect allowed transition (3.05 eV). Due to the low probability of

the direct forbidden transition, the indirect allowed transition dominates the optical absorption just above the absorption edge. The refractive index, n_D, of rutile is 2.609. Anatase has an indirect allowed transition at 3.2 eV and n_D of 2.488. Brookite is similar to anatase in which they both have indirect allowed transition—as there are only minor differences in their local crystal environment. The n_D of Brookite is 2.583. The amorphous and anatase phases of TiO_2 are preferred for the applications of optical coatings in visible range as they have wider band gap compared with rutile (narrower band gap of 3.05 eV at 406 nm wavelength) and higher absorption around 400 nm. Properties such as UV absorption and high refractive index in visible range are important for the design of interference optical coatings.

Various techniques have been used for the deposition of TiO_2 films, such as hydrothermal synthesis [9], plasma enhanced chemical vapor deposition (PECVD) [10], sol-gel [11], atomic layer deposition (ALD) [12], pulsed laser deposition (PLD) [13] and sputtering [7]. TiO_2 properties depend on the deposition process employed and process condition parameters. Using Monto Carlo simulation, Xiao et al. [14] have found that an atomically smooth surface can only be obtained within a certain deposition parameter window, at a regime of intermediate temperatures and low impingement rate. Tang et al. [7] produced single phase anatase and rutile using a reactive triode sputtering by controlling oxygen concentration and substrate temperature. These indicate that deposition methods and process parameters need to be carefully selected and optimized for a specific application as device performance will be significantly affected by the phase of TiO_2 and coating surface roughness.

Stereo/3D imaging has a wide range of applications, particularly in entertainment and games. Mehrabi et al. have provided an excellent review of 3D display including visual depth cues, technologies and their applications [15]. The concept of interest in this paper is binocular parallax of physiological depth cue, which fuses two slightly different images in human brain and provides 3D perception. This concept is currently widely used in TVs and cinemas. Various techniques can be used to realize to provide 3D perception based on binocular parallax [15,16], such as active stereo technique or passive stereo technique. The passive stereo technique uses polarizers or interference filters to separate images for left and right eye. Interference filter technique utilizes optical filter to pass only one or more specific wavelength bands and reflect the others, image separation is realized by wavelength difference. The advantages of interference filter technique for 3D display comparing to polarization technique include: nondepolarizing silver screens are not required [15]; image ghosting can be avoided; image resolution is maintained by using time sequential method even it is passive method [17]. Additional advantage is lower power consumption compared with polarization technique (when filters of glasses are well designed along with displayer, wavelength alignment) as polarizer only allows certain polarization light going through therefore reducing image brightness. Low power consumption becomes a more important factor as portable laser illuminated projector emerges on market [18]. On the other hand, this technique requires trained personnel to adjust the wavelengths of colors on the projectors; which increases costs [19].

Plasma assisted oxidation for a drum-based sputtering has been widely used in reactive thin film deposition processes for increasing productivity [20]. In this technique, the target material can be sputtered under metal-like conditions and further oxidized in highly reactive (oxygen or nitrogen) plasma area in a separated region; this allows high deposition rates while increasing the probability of obtaining stoichiometric oxides, furthermore this technique reduces possibility of target poisoning and provides better stability of process. Though TiO_2 sputtering processes have been investigated, the effects of process parameters on TiO_2 phases, surface structure and properties for this particular process are not well investigated. This paper investigated the influences of oxygen partial pressure and microwave power on TiO_2 structure and surface properties. Process parameters were optimized to achieve TiO_2 films with low surface scattering and absorption; then multi-passbands interference filter for 3D glasses were produced.

2. Experiments

Microwave plasma assisted magnetron pulse sputtering was chosen as the deposition process for this research. Two in-situ thickness monitoring methods are used in this system (broadband optical method and quartz crystal method), shown in Figure 1.

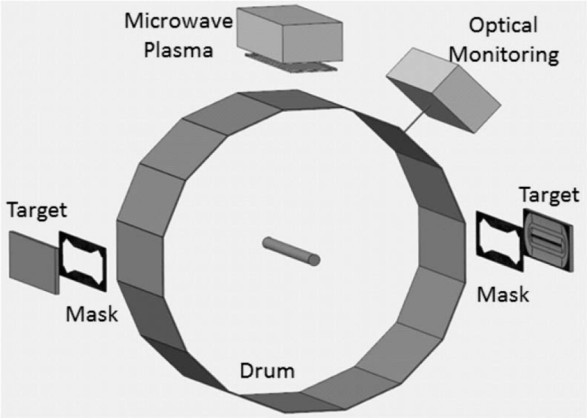

Figure 1. The schematic diagram of microwave assisted pulse DC drum-based sputtering system.

In this system, process takes place in two separate areas for deposition and oxidation, substrate mounted on a rotating drum that passes through sputter area to form a metal-like thin layer and then passes through microwave oxygen plasma area for further oxidation to form a fully oxidized thin film layer. In order to optimize process for producing high quality TiO_2 film for optical filters, a set of TiO_2 samples are deposited under various process parameters: varying microwave (MW) power and oxygen flow as listed in Table 1, other parameters are kept same.

Table 1. List of samples deposited under various conditions.

Sample	MW Power (kW)	O_2 Flow (sccm)
1	3	15
2	3	20
3	3	25
4	3	30
5	3	35
6	3	40
7	2.5	30
8	2	30

Samples are characterized using various techniques. Optical characterization data was acquired with a PerkinElmer Lambda 40 UV/Vis spectrometer (PerkinElmer, Waltham, MA, USA) measuring in transmission mode from 250–1100 nm. Raman and X-ray diffraction (XRD) were used for material and structure characterizations. Raman was done using Thermo Fisher Scientific—DXR Raman Microscope (Thermo Fisher Scientific, Waltham, MA, USA) equipped with lasers of 4 wavelengths (760 nm laser was used for this research); XRD was done using a Siemens D5100 Diffractometer (Siemens, Berlin, Germany) in locked-couple mode with 2θ range from 20°–30°. Scanning electron microscopy (SEM) and atomic force microscope (AFM) were also carried out for surface morphology analysis. Here, cross-sectional and top surface images were obtained using a Hitachi S4100 SEM (Hitachi, Tokyo, Japan) and the Dimension Icon AFM (Bruker, Billerica, MA, USA) in contact mode (with the tip OESTPA-R3 fitted) was used to analyses surface roughness.

3. Thin Film Modelling and Interference Filter Design

3.1. Dispersive Model Used for Transmittance Fitting

Dispersive function, n/k or dielectric constants versus wavelength, is needed for transmittance data fitting to obtain the n and k values for TiO_2 thin film required for thin film optical filter design. TiO_2 crystal is a direct band-gap semiconductor for rutile and brookite, anatase is an indirect band-gap semiconductor as the bottom of the conduction band (CB) is at Γ and the top of the valence band (VB) is at M [8]. However, the energy at Γ is only 0.18 eV lower than the top of the VB, therefore, Mo et al. [8] approximated anatase as a direct band-gap semiconductor. The eventual films produced in this work are mainly amorphous whose optical absorption behaves differently from a perfect crystalline semiconductor. The absorption edge of crystal semiconductor terminates abruptly at the energy gap, whereas the absorption of amorphous semiconductor does not stop at the energy gap and extends into the energy gap region. Thus the O'Leary-Johnson-Lim Model (OJL) model, a model for amorphous semiconductor, was employed to describe optical dispersion of dielectric function and carry out transmittance fitting [21]. OJL model assumes that the distribution of states/Density of Sates (DOS), $N(E)$, exhibits a square-root functional dependence in the band region and an exponential functional dependence in the tail region, described by the following equations:

$$N_C(E) = \frac{\sqrt{2}m_C^{*3/2}}{\pi^2\hbar^3}\begin{cases} \sqrt{E - V_C}, E \geq V_C + \frac{\gamma_C}{2} \\ \sqrt{\frac{\gamma_C}{2}}\exp\left(-\frac{1}{2}\right)\exp\left(\frac{E-V_C}{\gamma_C}\right), E < V_C + \frac{\gamma_C}{2} \end{cases} \quad (1)$$

$$N_V(E) = \frac{\sqrt{2}m_V^{*3/2}}{\pi^2\hbar^3}\begin{cases} \sqrt{\frac{\gamma_V}{2}}\exp\left(-\frac{1}{2}\right)\exp\left(\frac{E-V_V}{\gamma_V}\right), E \geq V_V - \frac{\gamma_V}{2} \\ \sqrt{E - V_V}, E < V_V - \frac{\gamma_V}{2} \end{cases} \quad (2)$$

The diagram of energy band structure of amorphous semiconductor as described by these equations are also shown in Figure 2, where the DOS of a perfect crystal follows a parabolic curve and its electronic band gap in can be derived as:

$$E_{g0} = V_C - V_V \quad (3)$$

V_c and V_v are ground state energies for the CB and VB. In amorphous semiconductors, the parameters of γ_v and γ_c are used to describe the tail-states for the valence and conduction bands respectively. The physical meaning γ_v and γ_c is disorder degree of amorphous material. For example, while $\gamma_c \to 0$, Equation (1) of conduction band DOS function gives the expression Equation (4). Similar results are also observed for the valence-band DOS function.

$$N_C(E) = \frac{\sqrt{2}m_C^{*3/2}}{\pi^2\hbar^3}\begin{cases} \sqrt{E - V_C}, E \geq V_C \\ 0, E < V_C \end{cases} \quad (4)$$

Using OJL model, the absorption coefficient of amorphous semiconductor can be obtained and therefore derive the extinction coefficient (k). The results of k can then be used to obtain the refractive index (n) by using the Kramers-Kronig relations (KKR). n and k against wavelength or energy of photon, dispersive function of amorphous semiconductor, is finally obtained. This dispersive function is then used to fit measured transmittance data and obtain the fitting parameters used in OJL model. Code software (W Theiss, version 3.5) was used to carry out transmittance fitting.

One important parameter, band gap E_{g0}, can be obtained by fitting measured transmittance data using OJL model. However, Tauc Plot [22] is also a commonly used method to find band-gap for crystal semiconductors using Equation (5):

$$\alpha h\nu = \beta(h\nu - E_g)^r \quad (5)$$

Here α is absorption coefficient; $h\gamma$ is photon energy; β is a constant; r is transition related parameter where $r = 1/2$ for direct allowed transitions, $r = 3/2$ for direct forbidden transitions, $r = 2$ for indirect allowed transitions and $r = 3$ for indirect forbidden transitions.

An extrapolation of a linear function of $(\alpha h\gamma)^{1/2}$ against $h\gamma$ [23] is used to define the energy gap of amorphous semiconductors. If using Equation (5), $r = 2$ can be used for amorphous transitions, which is same as indirect allowed transitions for crystal semiconductor. In this paper, energy band gaps will be obtained using both OJL model and Tauc plot as a comparison.

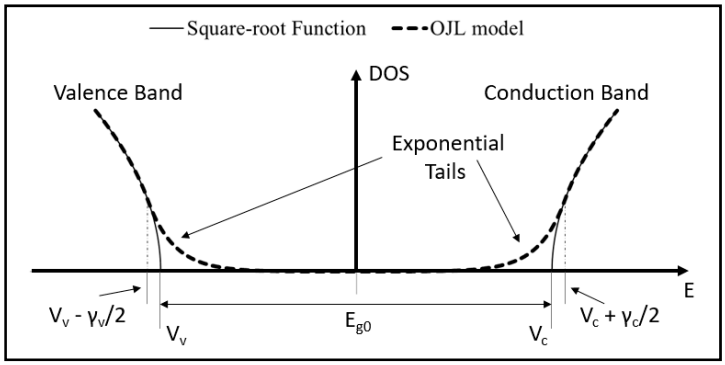

Figure 2. The diagram of energy band structure of amorphous semiconductor as described by Equations (1) and (2), thin solid curve: for crystal band structure; thick dash curve: for amorphous band structure.

3.2. Rough Surface and Light Scattering

The methods used for surface roughness treatment and the calculation of light scattering are based on the method from Rakels' paper [24], however, specular transmittance were derived instead of reflectance (Rakel et al. derived equations for reflectance). Light scattering can be considered as coherent scattering if surface roughness is much smaller than wavelength of measurement light. The electric field of light needs to be calculated by considering the phase modulation of electric field by rough surface profile. For simplification, normal incidence illumination is assumed in this paper as all transmittance measurements were carried out at normal incident in this research.

Gaussian distribution is used to describe surface roughness:

$$P(y) = \frac{1}{\sqrt{2\pi}R_q} \exp\left(-\frac{1}{2{R_q}^2}y^2\right) \tag{6}$$

In this function, y is surface height, the mean distribution is zero, R_q is the standard deviation. It can be found that R_q is also the root mean squared roughness of rough surface by integrating y^2 with Gaussian distribution.

Set $y = 0$ position as phase reference, where the initial phase is 0. Then the phase difference comparing to $y = 0$ is $\Delta = 2\pi y(n-1)/\lambda$ for the position with height y.

$$E = \int_{-\infty}^{\infty} \frac{1}{\sqrt{2\pi}R_q} \exp\left(-\frac{1}{2{R_q}^2}y^2\right) \cos\left(\frac{2\pi y(n-1)}{\lambda}\right) dy = \exp\left(-\frac{2(n-1)^2\pi^2{R_q}^2}{\lambda^2}\right) \tag{7}$$

The specular transmittance measured at normal direction is the ratio of light intensity, which is the squared modulus of electric field, then:

$$\frac{T_s}{T_0} = \exp\left[-\left(\frac{2\pi(n-1)R_q}{\lambda}\right)^2\right] \tag{8}$$

Here T_s is the specular transmittance for normal incident for rough surface, T_0 is the transmittance of smooth surface.

For a rough surface, light scattering effect is not the only effects to be considered. The rough surface also needs to be considered as a new layer consisting of a mixture of air and material (film or substrate). For example, Chen and Sun reported anti-reflection effect of nanostructured surface [25]. Effective Medium Approximation (EMA) was used to model the mixture layer of a rough surface and the Bruggeman model of EMA [26] is shown, Equation (9). The volume ratio of air to material can be assume 50% as roughness distribution is symmetric (Gaussian distribution).

$$f_1 \frac{\varepsilon_1 - \varepsilon}{\varepsilon_1 + 2\varepsilon} + f_2 \frac{\varepsilon_2 - \varepsilon}{\varepsilon_2 + 2\varepsilon} = 0 \quad (9)$$

ε_1 and ε_2 are dielectric function for air and material; ε is effective dielectric function of the mixture; and f_1 and f_2 are volume ratio, which is 50% here.

3.3. Design of Triple Bandpass Filter for 3D Glasses

Though the filter for 3D glasses is triple passbands, the design here is started from a single bandpass filter then advances to multi bandpass filter design. One of the most basic design formulas for a single bandpass filter is a single-cavity design which uses only one Fabry–Perot cavity [27]: substrate $|(HL)^n 2H(LH)^n|$ air, where H and L stand for high and low refractive index materials respectively. In this paper TiO_2 and SiO_2 were used as the high and low refractive index materials respectively (the index of TiO_2 is higher than the indices of ZrO_2, Nb_2O_5 and HfO_2, therefore providing high difference between H and L layer which may benefit the interference filter design). To improve the performance of bandpass filter, multi-cavities were used, the transmittance band approaches a rectangle as the number of cavities increases. To achieve an approximate multi-passbands transmittance shape as a start design, an adapted structure of multi-cavities of $(xHyL)^n$ 2H $(xLyH)^n$ was used. One example here: high index = 2.5 (roughly sputtered TiO_2 index at 550 nm) and low index = 1.45 (roughly sputtered SiO_2 index at 550 nm) and structure is $[(1.5H0.5L)^2$ 2H $(0.5L1.5H)^2$ L$]^3$ $(1.5H0.5L)^2$ 2H $(0.5L1.5H)^2$ with reference wavelength of 650 nm for design of side 1 of 3D glasses. Using this design as an initial structure, an optimized design was found using TFCalc software (version 3.5) and needle method within a few minutes. Transmittances of this design before and after optimization are shown in Figure 3a. Similarly, the triple passband filter design for side 2 of 3D glasses is also achieved, with reference wavelength at 700 nm. The optical density (OD = $-\log(T)$) performance are shown in Figure 3b for designs of both sides: ODs are higher than 3 for all necessary rejection bands.

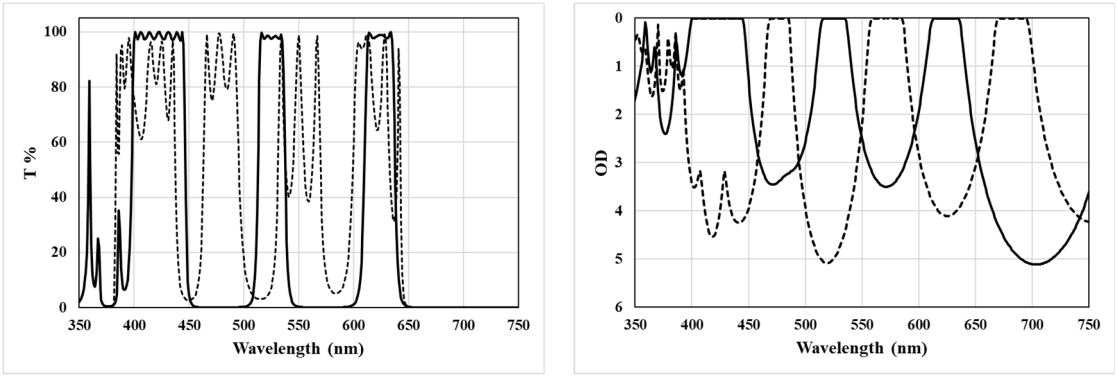

(**a**) (**b**)

Figure 3. (**a**) Transmittance for the design of side 1, dotted line: before optimization; solid line: after optimization; (**b**) Optical densities (ODs) of the designs for side 1 and side 2 of 3D glasses, solid line: side 1; dotted line: side 2.

4. Results and Discussions

4.1. TiO2 Thin Film Process Optimization

Two groups of TiO_2 samples were fabricated as described in the experimental session: fixed microwave power at 3 kW and varied oxygen flow; fixed oxygen flow at 30 sccm and varied microwave power. Transmittance of samples were measured. Figure 4a shows the transmittance for the samples with varying oxygen flows. It is clearly divided into 2 groups (insert of Figure 4a): higher light loss (dotted lines, 30, 35 and 40 sccm oxygen) and lower light loss (solid lines, 15, 20 and 25 sccm oxygen). In the second group, the sample deposited at 15 sccm oxygen has less transmittance than others. Figure 4b shows the transmittance for the samples with varying microwave power. It shows that transmittance varies with microwave power, sample at 3 kW microwave power has highest light loss. There are two possible reasons for light loss in transmittance measurement: absorption and scattering. To identify the reasons, further characterizations are carried out: XRD, Raman, SEM and AFM.

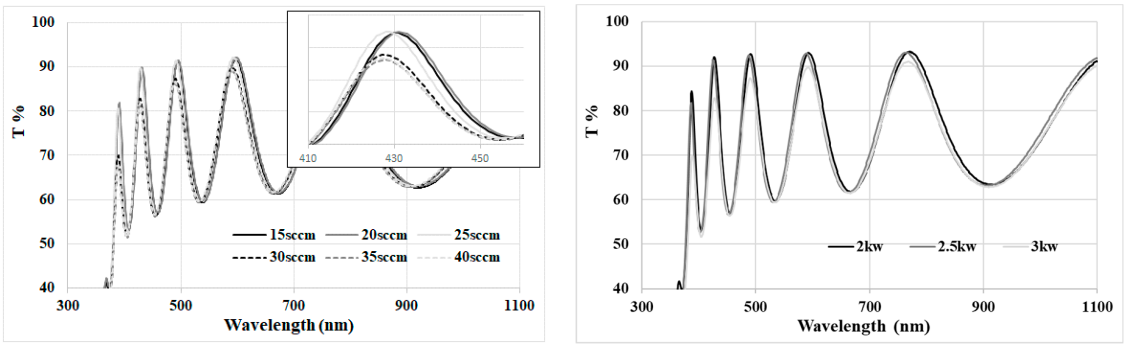

Figure 4. The transmittance for the samples with varying oxygen flows (**a**) and microwave power (**b**), the insert in (**a**) shows two groups of transmittances.

Cross-section and top surface of TiO_2 thin films are observed using SEM. The trends of surface morphology are: surface roughness increases while oxygen flow or microwave power increases. Figure 5 shows some SEM images of TiO_2 thin films deposited under various oxygen flows and microwave power.

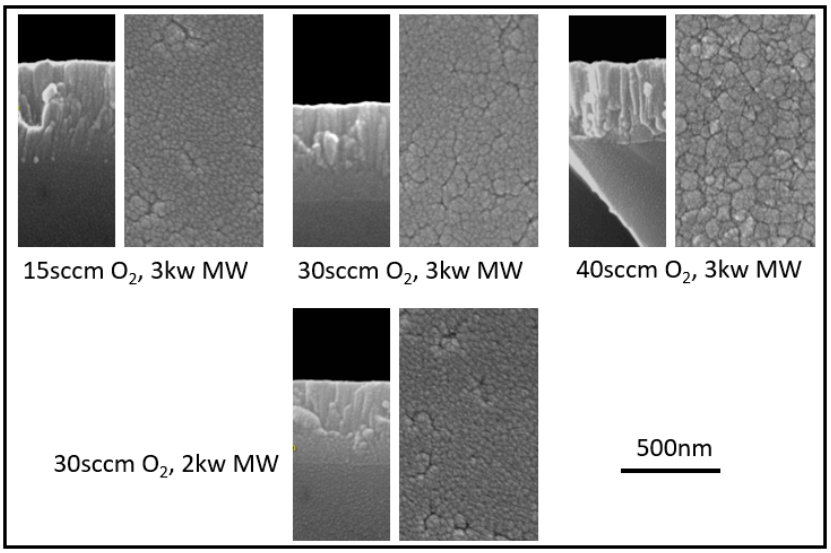

Figure 5. Scanning electron microscopy (SEM) images of TiO_2 thin films: cross-section and top surface.

However, SEM cannot give quantitatively surface roughness. AFM analysis (Figure 6) was also employed and the AFM results confirm the trends seen using SEM: surface roughness increases while oxygen flow or microwave power increases. Mean square root of surface roughness R_q of samples are listed in Table 2 and the R_q of bare substrate is 0.31 nm.

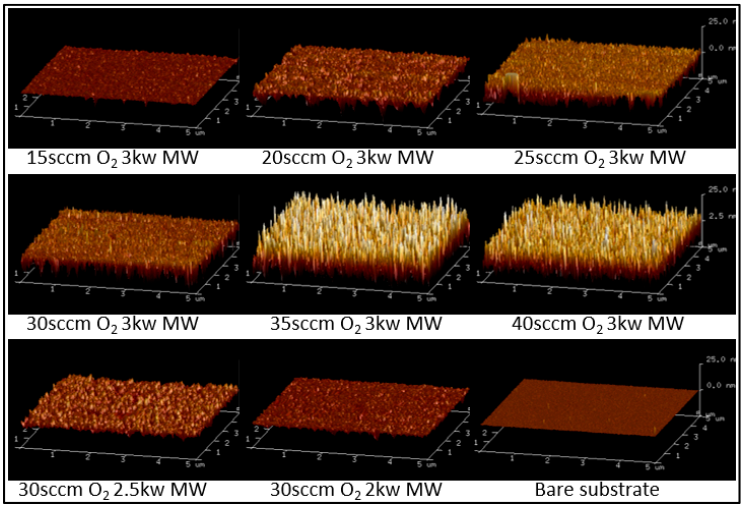

Figure 6. Atomic force microscopy (AFM) images of the samples with varying oxygen flows and microwave power.

Table 2. Mean square root of surface roughness R_q of TiO_2 thin films.

MW Power (kW)	O_2 Flow (sccm)	Roughness (R_q) (nm)
3	15	0.94
3	20	3.07
3	25	4.13
3	30	4.61
3	35	8.38
3	40	7.21
2.5	30	2.80
2	30	1.59

While it is intuitive to understand how the roughness varies with microwave power as microwave energy will roughen the surface, effects of oxygen content on roughness needed further analysis: XRD and Raman analysis were done.

XRD can be used to analyze the phase structure of TiO_2 thin films, such as anatase, rutile or amorphous. According XRD database, the strongest peaks of XRD (Cu Kα) are at 27.46° of 2θ for (110) rutile and at 25.35° of 2θ for (101) anatase [28]. Raman analysis can also demonstrate the phase structures of TiO_2 and their Raman active modes are well characterized. The anatase phase has six Raman active modes: a strong peak at 144 cm^{-1}, followed by peaks located at 197, 399, 513, 519 and 641 cm^{-1}; while the rutile phase has four active modes at 143, 236, 447 and 613 cm^{-1} [29].

XRD and Raman spectra for samples deposited under various oxygen flows at 3 kW microwave power are shown in Figure 7. In XRD, samples at 40 and 35 sccm oxygen flow showed anatase peak (25.35°), while the other samples did not show crystalline peaks. It can be seen that higher oxygen concentrations promote anatase formation, this agrees with the trend reported by Tang et al. [7] where pure anatase phase are obtained with oxygen concentration of 20%–30% and rutile phase obtained for oxygen concentration below 20%. In Raman spectra, samples at 40, 35 and 30 sccm oxygen flow showed anatase peak (144 cm^{-1}). This confirms the XRD results. In addition, the higher sensitivity of Raman spectroscopy compared with XRD for thin film measurements, showed detection of anatase

phase in the 30 sccm sample as well. The peak at 520 cm^{-1} seen in Figure 7b is due to crystalline silicon substrate.

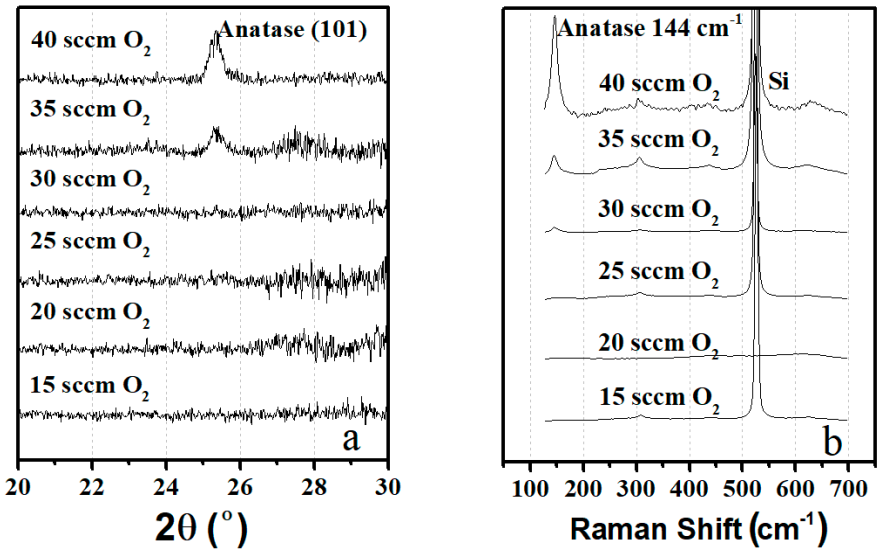

Figure 7. X-Ray diffraction (XRD) (**a**) and Raman (**b**) spectra of TiO_2 thin films deposited under various oxygen flows at 3 kW microwave power.

Samples with varied microwave power and fixed oxygen flow (30 sccm) did not show any peak in XRD measurements. For Raman measurements, anatase peak (144 cm^{-1}) was seen for samples at 3 and 2.5 kW but no anatase peak was seen for sample at 2 kW. This indicates that higher microwave power promotes anatase formation.

Based the analysis results from XRD, Raman and AFM, it can be concluded that the films contain a mixture of anatase crystal grains and amorphous TiO_2. Samples with higher anatase phase content also showed higher surface roughness, thus deducing that the formation of anatase grains can cause higher surface roughness.

According to above analysis, higher oxygen flow and higher microwave power will lead higher surface roughness. This increased surface roughness will reduce optical performance thin film. However, low oxygen flow and microwave power may result in partially oxidized thin film, causing high optical absorption. A model was constructed by considering surface roughness and OJL model for analysis, using layer stack of substrate/ideal TiO_2 layer/rough surface layer. For the rough surface layer, light scattering is taken into account while it is also treated as a thin film layer with complex refractive index (n and k) derived by using Bruggeman model (Equation (9)) with 50% volume fraction of air and TiO_2 mixture. The dispersive dielectric function of TiO_2 consists of dielectric background and one OJL model. Combining layer stack and dispersive function, measured transmittances of TiO_2 thin film samples were fitted. Parameter of layers and dispersive function were obtained and used to calculate n and k versus wavelength. For conciseness, only the parameters (obtained through data fitting) which are used for later discussion are listed in Table 3. The TiO_2 thicknesses, obtained through fitting, for all samples are around 490 nm. The optical fitted surface roughness R_q, obtained by using the Equation (8) in Section 3.2, are listed in Table 3, showing the same trend and similar level as the values obtained using AFM. Smoother surface is better for optical filter; however, the k value of film is also an important factor to consider when deciding process parameters; low k value give better optical filter performance. It is clear, therefore, that the best process parameters are 30 sccm oxygen flow and 2 kW microwave power for TiO_2 thin film deposition for our specific drum-based system.

As discussed, gap energy, E_{g0}, is one of the important physical parameters for optical thin films. OJL gap energies for TiO_2 thin films are listed in Table 3 as well. Values are higher than reported data. For comparison, Tauc Plot is also used to extrapolate gap energies where $r = 2$ for Equation (5) where

α values were calculated from fitted k values using $\alpha = 4\pi k/\lambda$. One of extrapolation fitting is shown in Figure 8 as example and gap energies obtained using Tauc Plot are listed in Table 4. These values are much closer to reported values for anatase phase, though still slightly higher.

Table 3. List of selected parameters obtained through data fitting for TiO_2 thin films.

Oxygen Flow (sccm)	MW Power (kW)	Gap Energy (eV)	Roughness (R_q, nm)	n @ 550 nm	k @ 550 nm
15	3	3.362	0.89	2.5063	0.0019
20	3	3.359	2.05	2.4974	0.0010
25	3	3.357	4.10	2.5057	0.0003
30	3	3.368	7.84	2.5007	0.0000
35	3	3.375	8.47	2.5027	0.0000
40	3	3.377	8.16	2.4943	0.0000
30	2.5	3.359	2.78	2.5021	0.0001
30	2	3.359	1.84	2.4952	0.0001

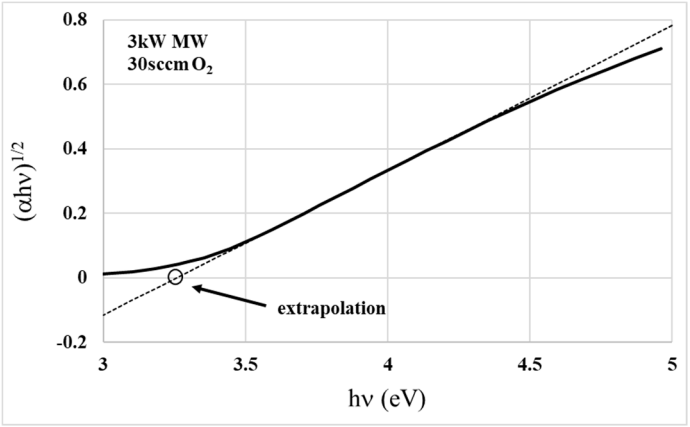

Figure 8. Example of one of the extrapolation fitting for obtaining gap energy using Tauc Plot.

Table 4. List of gap energies extracted using Tauc plot.

Oxygen Flow (sccm)	MW Power (kW)	Gap Energy (eV)
15	3	3.27
20	3	3.279
25	3	3.27
30	3	3.258
35	3	3.257
40	3	3.258
30	2.5	3.277
30	2	3.28

4.2. Fabrication of 3D Glasses Filter

Following discussions form the above sections, the process parameters for TiO_2 deposition were chosen to be 30 sccm oxygen flow and 2 kW microwave power. The n and k values for TiO_2 and SiO_2 used to produce 3D glasses filters are shown in Figure 9. These indices were used for replacing the constant index (2.5 for H layers and 1.45 for L layers in Section 3) in the initial designs. Then the initial designs of 3D glasses filters were re-optimized. The final design for side 1 has 49 layers with 4 um total thickness. The thinnest layer for side 1 is 24 nm. The final design for side 2 has 45 layers with 4.2 um total thickness. The thinnest layer for side 2 is 30 nm. The filters are deposited onto fused silica substrates, which are type JGS3 with index of 1.46 at wavelength of 550 nm and negligible absorption in the wavelength range of interest. Quartz crystals were used for in-situ thickness monitoring. Figure 10

shows the transmittance comparison between designs and measurements. It indicates thickness errors for both sides were controlled within the 0.5% range. It can also be seen that the transmittance discrepancies between design and measurement is larger for shorter wavelengths, this is due to more significant light scattering and absorption effects at shorter wavelengths. This effect can be more dominated by scattering.

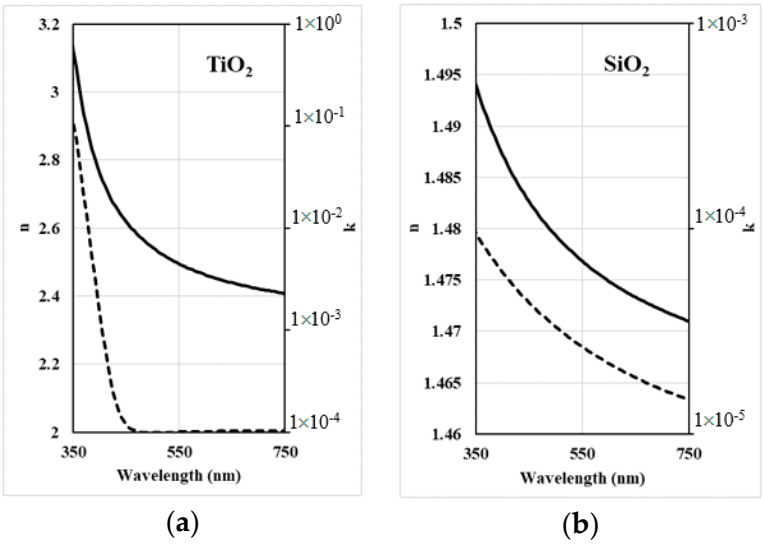

(**a**) (**b**)

Figure 9. The *n* and *k* values for TiO_2 (**a**) and SiO_2 (**b**) used to produce 3D glasses filters, solid line: *n*; dash line: *k*.

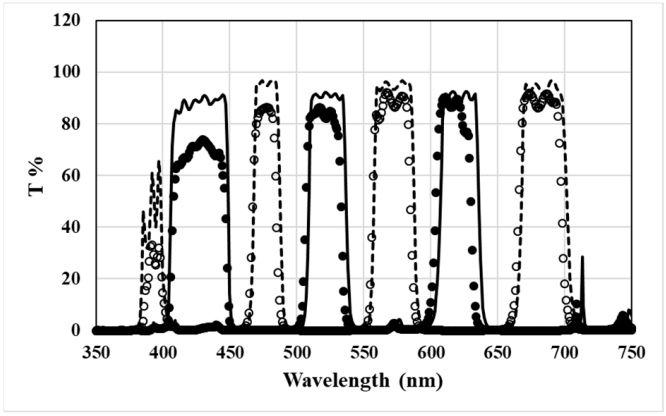

Figure 10. Transmittance of 3D glasses filters, solid line: side 1 design; solid circle: side 1 measurement; dotted line: side 2 design; open circle: side 2 measurement.

For numerical evaluation, the difference between a single layer and a multiple-layer structure need to be distinguished with regards to the characteristics of surface roughness. In Equation (8), only RMS (definition) of roughness parameter was considered, which would only be valid when the length between the lateral features of rough surface is very big, for example, the single layer surface roughness with reasonable thin thickness. However, for a multi-layer structure, particularly 45 layers or 49 layers structure in this paper, the feature of rough surface at lateral direction is much denser as roughness need to be considered for each interface and their effects accumulate. Thus, an additional parameter is used to define an arbitrary rough surface: autocovariance (ACV) length (l), describing lateral feature of a rough surface [30]. For normal incident of measurement light, when l is much

smaller than the wavelength (λ) of incident light, Equation (8) can be re-written by considering the effect of l for transmission using similar as used by Harvey et al. [30]:

$$\frac{T_s}{T_0} = \exp\left[-\left(\frac{2\pi(n-1)R_q}{\lambda}\right)^2\left[1-\exp\left(-\left(\frac{\pi l}{\lambda}\right)^2\right)\right]\right] \quad (10)$$

$$\frac{T_s}{T_0} \approx \exp\left[-\left(\frac{2\pi(n-1)R_q}{\lambda}\right)^2\left(\frac{\pi l}{\lambda}\right)^2\right] \quad (11)$$

$$\frac{T_s}{T_0} \approx 1-\left(\frac{2\pi(n-1)R_q}{\lambda}\right)^2\left(\frac{\pi l}{\lambda}\right)^2 \quad (12)$$

And, the transmission losses due to scattering when $l << \lambda$ can be obtained to be:

$$\Delta T \propto \frac{R_q^2 l^2}{\lambda^4} \quad (13)$$

For a more generic format of the equation, it can be written with n as power for wavelength:

$$\Delta T \propto \frac{R_q^2 l^2}{\lambda^n} \quad (14)$$

To summarize, Equation (8) is valid for describing scattering effects when $l >> \lambda$, while Equations (13) and (14) are better for describing scattering effects when $l << \lambda$.

To compare transmission losses, data was extracted from Figure 10 where ΔT is the difference of transmission percentage between design and measurement. This data was plotted and compared with the estimations using Equations (13) and (14). The plotted graph, Figure 11, shows that when $n = 4$, the trends agree very well, while $n = 6$ gave the best fitting.

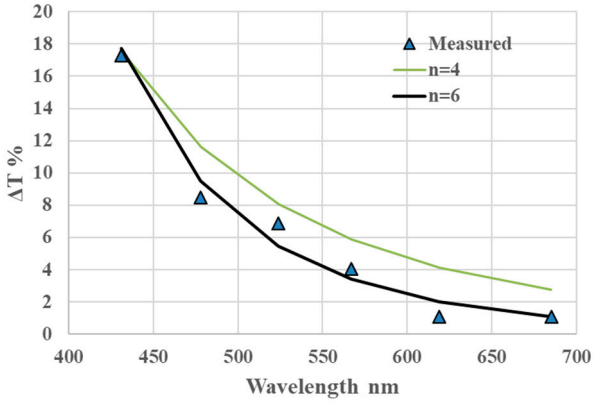

Figure 11. Comparison of transmission losses extracted from Figure 10, to transmission losses due to scattering using Equation (14), with different n values.

5. Conclusions

Two groups of TiO_2 samples were fabricated as described in the experimental session: fixed microwave power at 3 kW and varied oxygen flow; fixed oxygen flow at 30 sccm and varied microwave power. Their analysis, using SEM and AFM, showed surface morphology trend: surface roughness increases while oxygen flow or microwave power increases. Further analysis done using XRD and Raman showed presence of anatase phase. The results also indicated that higher microwave power and higher oxygen flow promotes anatase formation. Combining the analysis results from XRD, Raman

and AFM, it can be concluded that the samples with higher anatase phase content also showed higher surface roughness: thus, the formation of anatase grains can cause higher surface roughness.

Optical analysis of samples validates that higher oxygen flow and higher microwave power will lead to higher surface roughness. A compromise between surface roughness and fully oxidizing thin film required a modelling of process parameters: oxygen flow rate and microwave power. A model constructed by considering surface roughness and OJL model was used for analysis, to eventually obtain n, k and surface roughness parameters. The roughness parameters calculated from transmittance measurements agrees with AFM results. Balancing n, k and surface roughness for high performance optical thin films, the parameters for our TiO_2 process was chosen to be 30 sccm oxygen flow and 2 kW microwave power. The modelling done using OJL also provided information on gap energy, values obtained are higher than reported data. Tauc Plot is also used to extrapolate gap energies, these values are much closer to reported values for anatase phase, though still slightly higher.

Following analysis, the process parameters for TiO_2 deposition were chosen to be 30 sccm oxygen flow and 2 kW microwave power for fabricating 3D glasses filters. The transmittance measurement of the filters matched the designs very well: transmittance comparison between designs and measurements showed that thickness errors for both sides was controlled within 0.5% range.

Author Contributions: Conceptualization, S.S. and X.F.; Methodology, S.S. and Q.H.; Software, S.S.; Validation, S.S., D.G. and X.F.; Formal Analysis, Q.H and S.S.; Investigation, Q.H., S.S., X.F., D.G., C.L., H.O.C and Y.S.; Resources, S.S. and D.G.; Data Curation, H.Q., C.L. and S.S.; Writing-Original Draft Preparation, S.S. and H.Q.; Writing-Review & Editing, S.S.; Supervision, S.S. and X.F.

Funding: This research received no external funding.

Conflicts of Interest: The authors declare no conflict of interest.

References

1. Selopal, G.S.; Wu, H.-P.; Lu, J.; Chang, Y.-C.; Wang, M.; Vomiero, A.; Concina, I.; Diau, E.W.G. Metal-free organic dyes for TiO_2 and ZnO dye-sensitized solar cells. *Sci. Rep.* **2016**, *6*, 18756. [CrossRef] [PubMed]
2. Schneider, J.; Matsuoka, M.; Takeuchi, M.; Zhang, J.; Horiuchi, Y.; Anpo, M.; Bahnemann, D.W. Understanding TiO_2 photocatalysis: Mechanisms and materials. *Chem. Rev.* **2014**, *114*, 9919–9986. [CrossRef] [PubMed]
3. Tang, H.; Prasad, K.; Sanjinés, R.; Lévy, F. TiO_2 anatase thin films as gas sensors. *Sens. Actuators B Chem.* **1995**, *26*, 71–75. [CrossRef]
4. Keshavarz Hedayati, M.; Elbahri, M. Antireflective coatings: Conventional stacking layers and ultrathin plasmonic metasurfaces, a mini-review. *Materials* **2016**, *9*, 497. [CrossRef] [PubMed]
5. Lam, S.W.; Gan, W.Y.; Chiang, K.; Amal, R. TiO_2 semiconductor—A smart self-cleaning material. *J. Aust. Ceram. Soc.* **2008**, *44*, 6–11.
6. Verdier, T.; Coutand, M.; Bertron, A.; Roques, C. Antibacterial activity of TiO_2 photocatalyst alone or in coatings on *E. coli*: The influence of methodological aspects. *Coatings* **2014**, *4*, 670–686. [CrossRef]
7. Tang, H.; Prasad, K.; Sanjinès, R.; Schmid, P.E.; Lévy, F. Electrical and optical properties of TiO_2 anatase thin films. *J. Appl. Phys.* **1994**, *75*, 2042–2047. [CrossRef]
8. Mo, S.-D.; Ching, W.Y. Electronic and optical properties of three phases of titanium dioxide: Rutile, anatase, and brookite. *Phys. Rev. B* **1995**, *51*, 13023–13032. [CrossRef]
9. Chen, Q.; Qian, Y.; Chen, Z.; Wu, W.; Chen, Z.; Zhou, G.; Zhang, Y. Hydrothermal epitaxy of highly oriented TiO_2 thin films on silicon. *Appl. Phys. Lett.* **1995**, *66*, 1608–1610. [CrossRef]
10. Li, P.-Y.; Liu, H.-W.; Chen, T.-H.; Chang, C.-H.; Lu, Y.-S.; Liu, D.-S. Characterization of an amorphous titanium oxide film deposited onto a nano-textured fluorination surface. *Materials* **2016**, *9*, 429. [CrossRef] [PubMed]
11. Zabihi, F.; Ahmadian-Yazdi, M.-R.; Eslamian, M. Photocatalytic graphene-TiO_2 thin films fabricated by low-temperature ultrasonic vibration-assisted spin and spray coating in a sol-gel process. *Catalysts* **2017**, *7*, 136. [CrossRef]
12. Niemelä, J.-P.; Marin, G.; Karppinen, M. Titanium dioxide thin films by atomic layer deposition: A review. *Semicond. Sci. Technol.* **2017**, *32*, 093005. [CrossRef]

13. Murugesan, S.; Kuppusami, P.; Parvathavarthini, N.; Mohandas, E. Pulsed laser deposition of anatase and rutile TiO_2 thin films. *Surf. Coat. Technol.* **2007**, *201*, 7713–7719. [CrossRef]
14. Xiao, R.-F.; Ming, N.-B. Surface roughening and surface diffusion in kinetic thin-film deposition. *Phys. Rev. E* **1994**, *49*, 4720–4723. [CrossRef]
15. Mehrabi, M.; Peek, E.M.; Wuensche, B.C.; Lutteroth, C. Making 3D work: A classification of visual depth cues, 3D display technologies and their applications. In Proceedings of the Fourteenth Australasian User Interface Conference, Adelaide, Australia, 29 January–1 February 2013.
16. Holliman, N.S.; Dodgson, N.A.; Favalora, G.E.; Pockett, L. Three-dimensional displays: A review and applications analysis. *IEEE Trans. Broadcast.* **2011**, *57*, 362–371. [CrossRef]
17. Simon, A.; Prager, M.G.; Schwarz, S.; Fritz, M.; Jorke, H. Interference-filter-based stereoscopic 3D LCD. *J. Inf. Disp.* **2010**, *11*, 22–27. [CrossRef]
18. Reiners, D.; Rains, D.R.; Burgess, W.; Cruz-Neira, C. Laser illuminated projectors and their benefits for immersive environments. *Electron. Imaging* **2017**, *2017*, 42–47. [CrossRef]
19. Jorke, H.; Simon, A. New high efficiency interference filter characteristics for stereoscopic imaging. In *Stereoscopic Displays and Applications XXIII, Proceedings of IS&T/SPIE Electronic Imaging 2012, Burlingame, CA, USA, 22–26 January 2012*; Woods, A.J., Holliman, N.S., Favalora, G.E., Eds.; International Society for Optics and Photonics: Bellingham, WA, USA, 2012.
20. Song, S.; Li, C.; Chu, H.O.; Gibson, D. Reactive dynamics analysis of critical Nb_2O_5 sputtering rate for drum-based metal-like deposition. *Appl. Opt.* **2017**, *56*, C206. [CrossRef] [PubMed]
21. O'Leary, S.K.; Johnson, S.R.; Lim, P.K. The relationship between the distribution of electronic states and the optical absorption spectrum of an amorphous semiconductor: An empirical analysis. *J. Appl. Phys.* **1998**, *82*, 3334–3340. [CrossRef]
22. Tauc, J.; Grigorovici, R.; Vancu, A. Optical properties and electronic structure of amorphous germanium. *Phys. Status Solidi* **1966**, *15*, 627–637. [CrossRef]
23. Tauc, J. Optical properties of amorphous semiconductors. In *Amorphous and Liquid Semiconductors*; Springer: Boston, MA, USA, 1974; pp. 159–220.
24. Rakels, J.H. Influence of the surface height distribution on the total integrated scatter (TIS) formula. *Nanotechnology* **1996**, *7*, 43–46. [CrossRef]
25. Chen, J.Y.; Sun, K.W. Nanostructured thin films for anti-reflection applications. *Thin Solid Films* **2011**, *519*, 5194–5198. [CrossRef]
26. Stroud, D. The effective medium approximations: Some recent developments. *Superlattices Microstruct.* **1998**, *23*, 567–573. [CrossRef]
27. Macleod, H.A. Band-pass filters. In *Thin-Film Optical Filters*, 3rd ed.; Institute of Physics Publishing: Bristol, UK, 2001; p. 257. ISBN 0750306882.
28. Rafieian, D.; Ogieglo, W.; Savenije, T.; Lammertink, R.G.H. Controlled formation of anatase and rutile TiO_2 thin films by reactive magnetron sputtering. *AIP Adv.* **2015**, *5*, 097168. [CrossRef]
29. Sánchez, C.; Enrique, C. Quantification of phase content in TiO_2 thin films by Raman spectroscopy. *Superf. Vacío* **2014**, *27*, 88–92.
30. SHarvey, J.; Schröder, S.; Choi, N.; Duparré, A. Total integrated scatter from surfaces with arbitrary roughness, correlation widths, and incident angles. *Opt. Eng.* **2012**, *51*, 013402. [CrossRef]